Published in IET Generation, Transmission & Distribution
Received on 16th August 2011
Revised on 31st December 2011
doi: 10.1049/iet-gtd.2011.0539

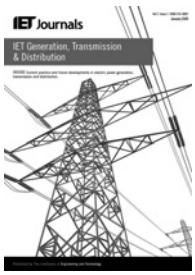

ISSN 1751-8687

Effects of the fault inception angle in fault-induced transients

F.B. Costa[1] *B.A. Souza*[2] *N.S.D. Brito*[2]

[1]*Federal University of Rio Grande do Norte – School of Science and Technology, Campus Universitário Lagoa Nova, Natal – RN, CEP:59.078-970, Brazil*
[2]*Department of Electrical Engineering, Federal University of Campina Grande, 882 Aprígio Veloso Av, Bodocongó, Campina Grande – PB, CEP:58.109-970, Brazil*
E-mail: flaviocosta@ect.ufrn.br

Abstract: The analysis of fault-induced transients in three-phase overhead transmission lines can provide extensive information about the fault type, detection, location, direction and sustained time in satisfactory agreement with real application in protective relays. These transients depend on the system topology, load condition and the fault parameters, such as the fault type, resistance, inception angle and location. This study addresses the fault inception angle effects in the energies of the fault-induced transients in both voltages and currents by means of the wavelet coefficient energy analysis at the first three wavelet scales, in which a generic energy equation regarding the fault-induced transients as a function of the fault inception angle in all kinds of faults was established.

1 Introduction

A transmission line is one of the most important components of the power system. A transmission line is very susceptive to faults because of its length. According to [1], about 80% of the power system faults take place on overhead three-phase lines. In this way, line protective systems are vital in order to minimise the harmful effects of the faults and improve the system stability.

Most conventional protection relays use fundamental-frequency components to detect and locate the faults [2]. Generally, a fault is cleared in about three power-frequency cycles [3]. However, the analysis of the high-frequency transients generated by faults (fault-induced transients) in protection measurements can provide high-speed fault clearance. These non-power-frequency components can present more information about the fault than power-frequency signals. In fact, the fault-induced transients contain extensive information about the fault type, location, direction and sustained time [4], ideal to design reliable methods for high-speed fault detection, classification and location in satisfactory agreement with real application in protective relays.

Fault currents at fault-clearing time in most transmission and distribution networks may be adequately represented by a power-frequency component, some harmonic components, an exponentially decaying DC component, fault-induced transients and noises [5]. With regard to the fault-induced transients, these components are presented in both the faulted voltages and currents soon after the fault inception time as a consequence of the travelling waves [6]. In addition, because of the mutual coupling effects in overhead three-phase transmission lines, voltages and currents in sound phases are also affected by the fault-induced transients [7]. The extraction of the fault-induced transients can allow high-speed fault detection, classification and location [8].

The features of the fault-induced transients depend on the system topology, load condition and the fault parameters, such as fault resistance, inception angle and location. The transient generated by faults have been the focus of much research [6, 7]. This paper addresses the fault-induced transient features as a function of the fault inception angle.

Taking into account all frequency components of the voltages and currents during the fault-clearing time, the fault-induced transient extraction may not be so easy. It is well-known that fault-induced transients are non-stationary in both time and frequency domains, with typical frequency spectrum from a few hundred Hz to various kHz [6, 7]. In this way, fault-induced transients can be properly extracted by using the wavelet transform [9], which divides the frequency spectrum, decomposing the signals into various components with distinct bandwidths (approximation and wavelet coefficients). Much research has been focused on wavelet-based techniques applied on detecting and classifying faults [10, 11] and estimating the fault location [12, 13].

In this paper, the fault-induced transient simulation is performed by using the real time digital simulator (RTDS) with a sampling frequency of 20 kHz. In this case, the wavelet coefficients of the first three scales are mainly influenced by the higher frequency components of the signals and can be used in order to identify the fault-induced transient features. These coefficients may be predominantly influenced by the transient-generated by faults.

In this paper, the fault inception angle effects in the energies of fault-induced transients are obtained by means of the wavelet coefficient energy analysis. With the range of frequency of interest, from 1.25 to 10 kHz (the first three scales), a generic wavelet coefficient energy equation (energy regarding the fault-induced transients) of both voltages and currents as a function of the fault inception angle in all kinds of faults was established. Advantages and disadvantages of the wavelet coefficient energy (energy regarding fault-induced transients) analysis for high-speed fault detection, classification and location is also dealt with in this paper.

This paper is organised as follows: Section 1: Introduction; Section 2: Definition of the wavelet coefficient energy; Section 3: Real-time simulation of the faults; Sections 4–7: The effects of the fault inception angle in the energy of the wavelet coefficients related to the fault-induced transients in single line-to-ground (SLG), line-to-line (LL), double line-to-ground (DLG), and three line faults, respectively; Section 8: Practical application of the wavelet coefficient energies; Section 9: Conclusion.

2 Energy of the wavelet coefficients

A suitable way to extract information regarding the frequency contents of transients in voltages and currents is by using a time–frequency signal decomposition such as the well-known short-time Fourier transform (STFT). However, the STFT uses a fixed-size window which can limit the analysis of some non-stationary signals. To overcome some drawbacks of the STFT, the wavelet transform has been successfully used for analysing non-stationary signals in power system applications, providing difference frequency resolution while preserving time and frequency information (multi-resolution analysis).

The wavelet transform is a well-known powerful tool to analyse a signal within different frequency ranges, by dilating and translating a single function named mother wavelet [14]. Besides the discrete wavelet transform (DWT), the maximal overlap discrete wavelet transform (MODWT) also uses low- and high-pass filters (scale and wavelet filters) to divide the frequency-band of the input signal into low- and high-frequency components (approximation and wavelet coefficients). This operation may be repeated recursively, feeding the low-pass filter output into another identical filter pair, decomposing the signal into approximation and wavelet coefficients at various scales. However, in contrast to the DWT, there is no down-sampling in MODWT (time-invariant transformation) [15]. In this way, the fault-induced transients can be detected faster by means of the MODWT [9].

The coefficients of the scale and wavelet filters and their frequency responses are associated with the selected mother wavelet. According to [16], the wavelet Daubechies 4 (db4) provides an accurate detection of the fast transients in power systems. In this paper, the wavelet coefficients are computed through the MODWT with db4.

According to the theorem of Parseval, the energy of a signal can be decomposed in terms of the energy of the wavelet coefficients at scales $j = \{1, 2, \ldots, J\}$ and the energy of the approximation coefficients at the scale J of the MODWT [15], as follows

$$\sum_{k=1}^{k_t} |x(k)|^2 = \sum_{k=1}^{k_t} |c_J(k)|^2 + \sum_{j=1}^{J} \sum_{k=1}^{k_t} |w_j(k)|^2 \qquad (1)$$

where x is the original signal; c_J are the approximation coefficients at scale J; w_j are the wavelet coefficients at scale $j \le J$; $\sum_{k=1}^{k_t} |x(k)|^2$ is the energy of the signal; $\sum_{k=1}^{k_t} |c_J(k)|^2$ is the approximation coefficient energy at scale J; $\sum_{k=1}^{k_t} |w_j(k)|^2$ is the wavelet coefficient energy at scale j; k_t is the total amount of samples of the original signal.

Some features of fault-induced transients can be identified through the analysis of their energy. Since the energy of the signal can be decomposed in terms of the wavelet coefficient energy at various scales, the features of the transients can be identified through the analysis of the wavelet coefficient energy at some scales, specially when the wavelet coefficients are predominantly influenced by frequency components regarding the fault-induced transients.

The wavelet coefficient energy ($\mathcal{E}$) of a signal (voltage or current), at the scale j, is computed at sample k_i taking into account the last wavelet coefficients in one cycle (one-cycle window) as follows

$$\mathcal{E}_j = \sum_{k=k_i-\Delta k}^{k_i} |w_j(k)|^2 \qquad (2)$$

where w_j are the wavelet coefficients of the signal (voltage or current) at the scale j; $\Delta k = f_s/f$ is the coefficient amount equivalent to one cycle of the fundamental power frequency (f); f_s is the sampling frequency.

3 Fault simulation

In order to evaluate the fault inception angle effects in fault-induced transients, a simplified transmission system (Fig. 1) was modelled and simulated by using the RTDS. The system is composed of a typical 230 kV, 180 km transmission line of Chesf (a Brazilian power utility), connected to a source at the sending end (bus 1) and a load at the receiving end (bus 2).

Faults with fault resistance $r_f = 10\ \Omega$, fault location $d_f = 90$ km from bus 1 (at the middle of the line), fault inception angle $\theta_f = \{0, 1, 2, \ldots, 179\}$ electrical degrees and fault type = {*AG*, *BG*, *CG*, *AB*, *BC*, *CA*, *ABG*, *BCG*, *CAG* and *ABC*} were simulated (1800 fault simulations). Both r_f and d_f were taken as constant in order to avoid the influence of these parameters in the fault inception angle.

In each fault simulation, voltages and currents at the fault location (v_{Af}, v_{Bf}, v_{Cf}, v_{Nf}, i_{Af}, i_{Bf}, i_{Cf} and i_{Nf}) and voltages and currents at the bus 1 (v_A, v_B, v_C, v_N, i_A, i_B, i_C and i_N) were obtained. Therefore 3600 records were assessed. In this paper, the fault inception angle θ_f is the phase angle of the voltage v_{Af} at the fault inception time.

In order to identify how the energy of the fault-induced transients changes with the fault inception angle, the wavelet coefficient energies of the MODWT of the voltages

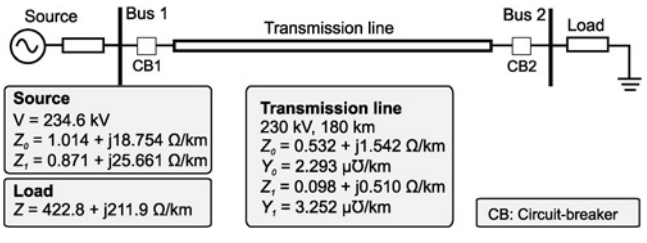

Fig. 1 *Simplified power transmission system model*

IET Gener. Transm. Distrib., 2012, Vol. 6, Iss. 5, pp. 463–471
doi: 10.1049/iet-gtd.2011.0539

and currents, at the fault location, for each simulated fault ($\mathcal{E}_{v_{Af}}$, $\mathcal{E}_{v_{Bf}}$, $\mathcal{E}_{v_{Cf}}$, $\mathcal{E}_{v_{Nf}}$, $\mathcal{E}_{i_{Af}}$, $\mathcal{E}_{i_{Bf}}$, $\mathcal{E}_{i_{Cf}}$ and $\mathcal{E}_{i_{Nf}}$) were assessed. These energies were computed by (2), at the first scale, with $k_i = k_f + \Delta k$. In this way, the wavelet coefficients from k_f to $k_f + \Delta k$ (one cycle length) were taken into account. In the same way, the wavelet coefficient energies of the voltages and currents at the bus 1 for each simulated fault ($\mathcal{E}_{v_A}$, $\mathcal{E}_{v_B}$, $\mathcal{E}_{v_C}$, $\mathcal{E}_{v_N}$, $\mathcal{E}_{i_A}$, $\mathcal{E}_{i_B}$, $\mathcal{E}_{i_C}$ and $\mathcal{E}_{i_N}$) were also assessed. These energies were computed by (2), at the first scale, taking into account the wavelet coefficients from k_1 to $k_1 + \Delta k$.

The simulation time step used by the RTDS is 50 μs and all signals were sampled with $f_s = 20$ kHz.

4 Fault inception angle effects in single line-to-ground faults

Taking into account a balanced three-phase transmission system, the phase voltages at the point of fault, at the fault inception time are

$$v_f(\theta_f) = V \sin(\theta_f + \delta) \tag{3}$$

where $v_f = \{v_{Af}, v_{Bf}$ or $v_{Cf}\}$; phase voltages are phase-shifted by 120 electrical degrees. In this way, the phase angle of the voltages are $\delta = \{\delta_A, \delta_B$ and $\delta_C\} = \{0^\circ, -120^\circ$ and $120^\circ\}$ in $v_f = \{v_{Af}, v_{Bf}$ and $v_{Cf}\}$, respectively.

The worst fault-induced transient condition in both voltages and currents in SLG faults corresponds to the fault striking in the voltage peak [6]. Therefore the fault-induced transients are more severe when

$$\theta_f = 90^\circ - \delta \pm n180^\circ \tag{4}$$

where $n = \{0, 1, 2, \ldots\}$. With regard to the *AG*, *BG* and *CG* faults, the worst fault-induced transients take place when $\theta_f = 90^\circ$, 30° and 150°, respectively.

Fig. 2 depicts v_{Af} and v_A of the simulated *AG* faults with $\theta_f = 30^\circ$ and $\theta_f = 90^\circ$. The fault-induced transients in v_A were more severe when $\theta_f = 90^\circ$ than $\theta_f = 30^\circ$ because of the hard decrease in voltage at the sine wave peak in v_{Af}. The severity of the fault-induced transients can be identified through the magnitude of their energies: the higher value of the energy of the transients is related to the most severe transients.

At the point of fault, the sample regarding the fault inception time is k_f, which corresponds to phase angle θ_f in voltage v_{Af}. However, because of the transit time of the travelling waves from the fault location to bus 1, the transients regarding the fault-inception time are detectable from sample k_1, at the bus 1, where $k_1 > k_f$. At sample k_1,

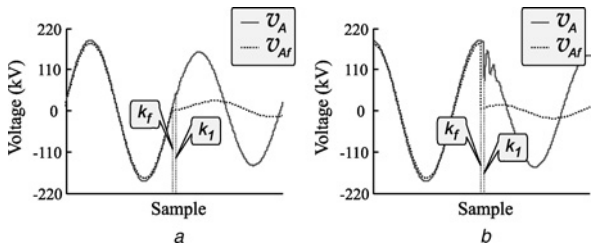

Fig. 2 *Fault inception angle effects in voltages at both the fault location and bus 1, in AG faults*

a $\theta_f = 30^\circ$
b $\theta_f = 90^\circ$

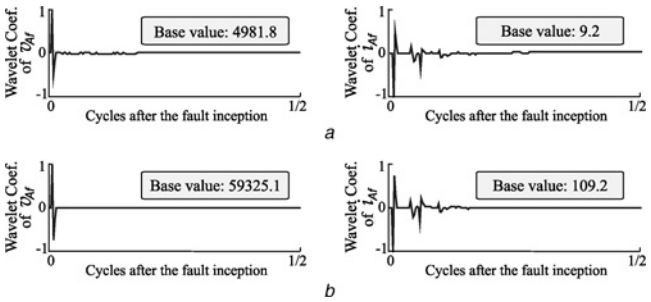

Fig. 3 *Normalised wavelet coefficients of the phase A voltage and current in AG fault at the fault location*

a $\theta_f = 30^\circ$
b $\theta_f = 90^\circ$

the phase angle in voltage v_A is $\theta_f + \Delta\theta$, where $\Delta\theta$ is the phase angle equivalent to $k_1 - k_f$ (a function of the fault location).

Fig. 3 depicts the normalised wavelet coefficients of v_{Af} (Fig. 2) and i_{Af} of the simulated *AG* faults with $\theta_f = 30^\circ$ and $\theta_f = 90^\circ$ (coefficients regarding the first half-cycle of the fault-induced transients). By using the wavelet coefficients at various scales, the following features were observed in voltages and currents (all phases and neutral), in all types of faults:

- The frequency spectrum of the fault-induced transients does not change with θ_f (the wavelet coefficient waveforms did not change significantly with θ_f, such as shown in Fig. 3).
- The magnitude of the wavelet coefficients changes with θ_f (Fig. 3). As a consequence, the magnitude of the fault-induced transients and the energy of these transients change with θ_f.
- These features were also observed in [7] by using the Fourier analysis. However, this paper provides a throughout analysis of the effects of θ_f in the energies of the fault-induced transients for all types of faults by using the wavelet transform. These analyses are very important for developing fault diagnosis methods based on the analysis of either fault-induced transients or travelling waves.
- In order to identify how the energy of the fault-induced transients changes with θ_f in SLG faults and the severity of these transients, the wavelet coefficient energies at the point of the fault and at the bus 1 were assessed. Fig. 4 depicts the energies related to the voltages in *AG* faults ($\mathcal{E}^{AG}_{v_{Af}}(\theta_f)$, $\mathcal{E}^{AG}_{v_{Bf}}(\theta_f)$, $\mathcal{E}^{AG}_{v_{Cf}}(\theta_f)$, $\mathcal{E}^{AG}_{v_{Nf}}(\theta_f)$, $\mathcal{E}^{AG}_{v_A}(\theta_f)$, $\mathcal{E}^{AG}_{v_B}(\theta_f)$, $\mathcal{E}^{AG}_{v_C}(\theta_f)$ and $\mathcal{E}^{AG}_{v_N}(\theta_f)$).

By using the regression analysis through the Curve Fitting Toolbox of Matlab® with standard Levenberg–Marquardt curve fit, a single equation regarding the wavelet coefficient energy waveforms of all the voltages and currents in *AG*, *BG* and *CG* faults was obtained, as follows

$$\mathcal{E}(\theta_f) = E_0 + E_1 \sin^2(\theta_f + \delta_E) \tag{5}$$

where E_0 and E_1 are energy magnitudes whose values depend on the fault location, fault resistance, system parameters, mother wavelet, wavelet scale and the length of the energy window which remained constant in simulations; $\delta_E = \{\delta_A, \delta_B, \delta_C\} = \{0^\circ, -120^\circ, 120^\circ\}$ in *AG*, *BG* and *CG* faults, respectively, according to the value of δ in (3). Fig. 4 depicts also the values of E_1 and δ_E obtained through the

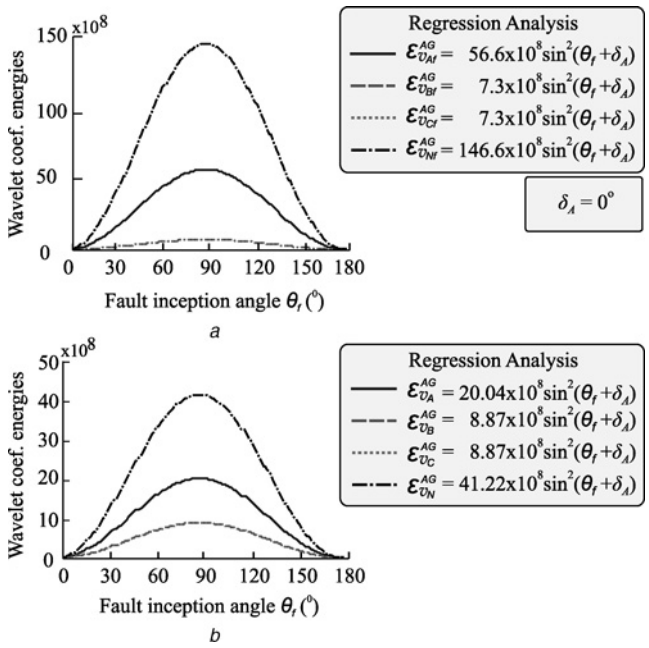

Fig. 4 *Wavelet coefficient energies of the voltages in AG faults*
a $\mathcal{E}^{AG}_{v_{Af}}(\theta_f)$, $\mathcal{E}^{AG}_{v_{Bf}}(\theta_f)$, $\mathcal{E}^{AG}_{v_{Cf}}(\theta_f)$ and $\mathcal{E}^{AG}_{v_{Nf}}(\theta_f)$
b $\mathcal{E}^{AG}_{v_A}(\theta_f)$, $\mathcal{E}^{AG}_{v_B}(\theta_f)$, $\mathcal{E}^{AG}_{v_C}(\theta_f)$, and $\mathcal{E}^{AG}_{v_N}(\theta_f)$

regression analysis in *AG* faults. Regarding the *BG* and *CG* faults, the features of the energies were similar to *AG* faults. For instance, the energies related to the voltages at the point of the fault were

$$\mathcal{E}^{BG}_{v_{Af}} \simeq 7.3\times10^8\sin^2(\theta_f+\delta_B),$$
$$\mathcal{E}^{BG}_{v_{Bf}} \simeq 56.7\times10^8\sin^2(\theta_f+\delta_B)$$
$$\mathcal{E}^{BG}_{v_{Cf}} \simeq 7.3\times10^8\sin^2(\theta_f+\delta_B), \quad \text{and}$$
$$\mathcal{E}^{BG}_{v_{Nf}} \simeq 146.9\times10^8\sin^2(\theta_f+\delta_B)$$

for BG faults and

$$\mathcal{E}^{CG}_{v_{Af}} \simeq 7.3\times10^8\sin^2(\theta_f+\delta_C),$$
$$\mathcal{E}^{CG}_{v_{Bf}} \simeq 7.3\times10^8\sin^2(\theta_f+\delta_C)$$
$$\mathcal{E}^{CG}_{v_{Cf}} \simeq 56.7\times10^8\sin^2(\theta_f+\delta_C), \quad \text{and}$$
$$\mathcal{E}^{CG}_{v_{Nf}} \simeq 146.8\times10^8\sin^2(\theta_f+\delta_C)$$

for CG faults.

The energy waveforms regarding the SLG faults were obtained with $R^2 \simeq 0.9998$ (square of the multiple correlation coefficient).

After the analysis of the wavelet coefficient energy waveforms of *AG* (Fig. 4), *BG* and *CG* faults, it was verified that [8]:

- The wavelet coefficient energies regarding the fault-induced transients in all voltages and currents along the line in SLG faults are square sinusoidal functions of the fault inception angle according to (5).
- The energy peak (the hardest fault-induced transients) in all energy waveforms is in accordance with (4).
- There is a fault inception angle where the wavelet coefficient energy values are about zero (no fault-induced transients [11]). As a consequence, in *AG* faults, for instance, algorithms based on the fault-induced transient or travelling wave analysis to detect and locate faults may fail when the fault inception angle is near zero degree.
- Owing to the mutual coupling effects between the line phases, voltages and currents in sound phases are also affected by the fault-induced transients [7]. However, as expected, in *AG* faults, for instance, the energy waveforms regarding the faulted voltages ($\mathcal{E}^{AG}_{v_A}$ and $\mathcal{E}^{AG}_{v_N}$) and currents ($\mathcal{E}^{AG}_{i_A}$ and $\mathcal{E}^{AG}_{i_N}$) are well distinguished from the sound voltages ($\mathcal{E}^{AG}_{v_B}$ and $\mathcal{E}^{AG}_{v_C}$) and currents ($\mathcal{E}^{AG}_{i_B}$ and $\mathcal{E}^{AG}_{i_C}$). As a consequence, the wavelet coefficient energies (or the fault-induced transients) at line ends can be properly used for fault classification purpose.
- Fig. 5 depicts the energy waveforms $\mathcal{E}^{AG}_{i_{Af}}(\theta_f)$, $\mathcal{E}^{AG}_{i_{Bf}}(\theta_f)$, $\mathcal{E}^{AG}_{i_{Cf}}(\theta_f)$ and $\mathcal{E}^{AG}_{i_{Nf}}(\theta_f)$ at the first three scales in *AG* faults. The wavelet coefficient energies of the voltages and currents at various scales in all SLG faults were evaluated and it was observed that [8]:
- The wavelet coefficient energies regarding the fault-induced transients within a wideband are square sinusoidal functions of the fault inception angle according to (5).
- Taking into account the sampling frequency of $f_s = 20$ kHz, the wavelet coefficient energy magnitude was higher in the first scale. In this way, the analysis of the wavelet coefficient energies in the first scale may result in a better fault detection. In addition, the use of the first scale can provide a high speed fault-induced transient detection in agreement with real-time applications in protective relays [9].

Various Daubechies, Symlet and Coiflet wavelets were evaluated and the main features of the previously discussed wavelet coefficient energies were not influenced with the mother wavelet families.

Based on both the obtained wavelet coefficient energy features and the theorem of Parseval, the energy of the fault-induced transients of the voltages and currents along the line may be a square sinusoidal function of the fault inception angle and may present similar features of the addressed wavelet coefficient energy.

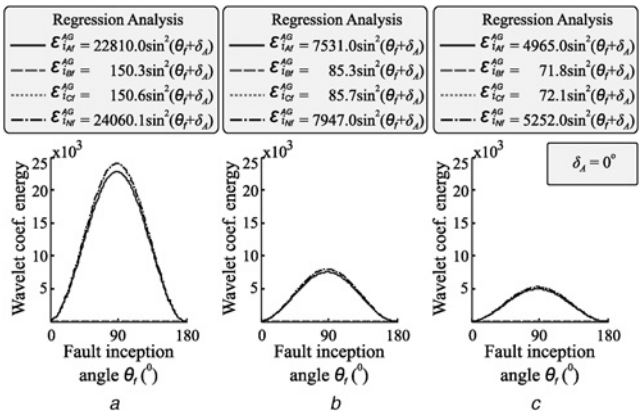

Fig. 5 *Wavelet coefficient energies of the currents at the fault location in AG faults*
a Scale 1
b Scale 2
c Scale 3

doi: 10.1049/iet-gtd.2011.0539

5 Fault inception angle effects in line-to-line faults

As analogy to the SLG faults, the wavelet coefficient energies of the fault-induced transients in LL faults may be a function of the point on wave where the fault strikes at line voltages. Taking into account a balanced three-phase system, the line voltages at the point of fault, at the fault inception time are

$$v_f(\theta_f) = \sqrt{3}V \sin(\theta_f + \delta + 30^\circ) \quad (6)$$

where $v_f = \{v_{ABf}, v_{BCf}$ or $v_{CAf}\}$; line voltages are phase-shifted by 120°. Therefore the phase angle of the voltages are $\delta = \{\delta_A, \delta_B$ and $\delta_C\} = \{0^\circ, -120^\circ$ and $120^\circ\}$ in $v_f = \{v_{ABf}, v_{BCf}$ and $v_{CAf}\}$, respectively. As alternative, (6) can be rewritten as follows

$$v_{ABf}(\theta_f) = \sqrt{3}V \sin(\theta_f + \delta_{AB}) \quad (7)$$

$$v_{BCf}(\theta_f) = \sqrt{3}V \sin(\theta_f + \delta_{BC}) \quad (8)$$

$$v_{CAf}(\theta_f) = \sqrt{3}V \sin(\theta_f + \delta_{CA}) \quad (9)$$

where $\{\delta_{AB}, \delta_{BC}, \delta_{CA}\} = \{\delta_A, \delta_B, \delta_C\} + 30^\circ = \{30^\circ, -90^\circ, 150^\circ\}$.

As analogy to the *AG* faults, the worst fault-induced transient condition in both voltages and currents in AB faults corresponds to the fault striking in $\theta_f + 0^\circ + 30^\circ = 90^\circ \Rightarrow \theta_f = 60^\circ$. On the other hand, the more damped fault-induced transients take place in $\theta_f + 60^\circ \pm 90^\circ \Rightarrow \theta_f = -30^\circ$ or $\theta_f = 150^\circ$.

In AB faults, the voltage v_{ABf} is taken as reference to identify the effects of the fault inception angle in fault-induced transients, computed as follows

$$v_{ABf} = v_{Af} - v_{Bf} = V \sin(\theta_f) - V \sin(\theta_f - 120^\circ) \quad (10)$$

or

$$v_{ABf} = \frac{\sqrt{3}}{2} V \sin(\theta_f + 30^\circ) - \left(-\frac{\sqrt{3}}{2} V \sin(\theta_f + 30^\circ)\right) \quad (11)$$

where $\sqrt{3}/2V \sin(\theta_f + 30^\circ)$ and $-(\sqrt{3}/2)V \sin(\theta_f + 30^\circ)$ are the projections of the phasors v_{Af} and v_{Bf} at the direction of the phasor v_{ABf}, termed in this paper as $v_{Af/ABf}$ and $v_{Bf/ABf}$, respectively.

Fig. 6 depicts the phasor v_{ABf} as a result of both $v_{Af} - v_{Bf}$ and $v_{Af/ABf} - v_{Bf/ABf}$ in an *AB* fault with $\theta_f = 90^\circ$. In this case, the fault took place 90° in phase *A* voltage and 330° in phase *B* voltage (distinct points on fault voltage waveforms) which would generate distinct fault-induced transients according to the Section 4. However, in *AB* faults the ground is not taken as reference, the phasor v_{ABf} is the reference. According to Fig. 6, $v_{ABf} = v_{Af} - v_{Bf} = v_{Af/ABf} - v_{Bf/ABf}$ and $v_{Af/ABf} = -v_{Bf/ABf}$ for all possible fault inception angles. As a consequence, at *AB* fault axe, the fault-induced transients in each faulted voltage (phases *A* and *B*) present about the same magnitude in modulus with different polarities. In this way, the energy values of these transients are the same. Similar features are expected in the energy of the fault-induced transients of the phase *A* and *B* currents.

Owing to mutual coupling between the transmission line conductors, both the fault phases produce fault-induced transients in the sound phase (phase *C*). These transients

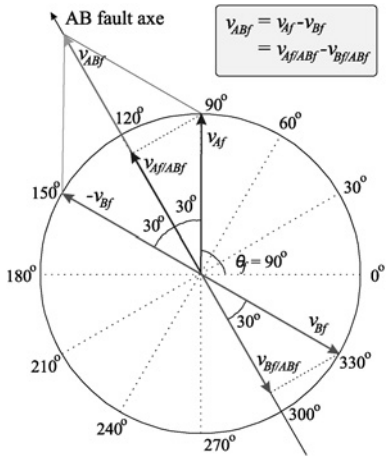

Fig. 6 *Line voltage between the phases A and B in an AB fault with fault inception angle of 90°*

are combined according to the travelling wave superposition principium. Taking into account the ideally transposed line, the fault-induced transients in the sound phase are near zero because the magnitude of the fault-induced transients in faulted phases is equal in modulus with different polarities. As a consequence, the wavelet coefficient energies of the voltage and current in the sound phase and neutral may be null.

In order to identify how the energy of the fault-induced transients changes with θ_f in LL faults, the wavelet coefficient energies at the fault location and at bus 1 were assessed. Fig. 7 depicts the energy waveforms for *AB* faults at the fault location ($\mathcal{E}^{AB}_{v_{Af}}, \mathcal{E}^{AB}_{v_{Bf}}, \mathcal{E}^{AB}_{v_{Cf}}, \mathcal{E}^{AB}_{v_{Nf}}, \mathcal{E}^{AB}_{i_{Af}}, \mathcal{E}^{AB}_{i_{Bf}}, \mathcal{E}^{AB}_{i_{Cf}}$ and $\mathcal{E}^{AB}_{i_{Nf}}$).

By using regression analysis through the Curve Fitting Toolbox of Matlab®, (5) was also true to the wavelet coefficient energies regarding the *AB* (Fig. 7), AC and BC faults monitored at both bus 1 and the fault point. It was obtained $\delta_E = \{\delta_{AB}, \delta_{BC}$ and $\delta_{CA}\} = \{30^\circ, -90^\circ$ and $150^\circ\}$ in *AB*, *BC* and *CA* faults, respectively. Fig. 7 depicts also the values of E_1 and δ_E obtained through the regression analysis. Regarding the *BC* and *CA* faults, the features of the energies were similar to *AB* faults. For

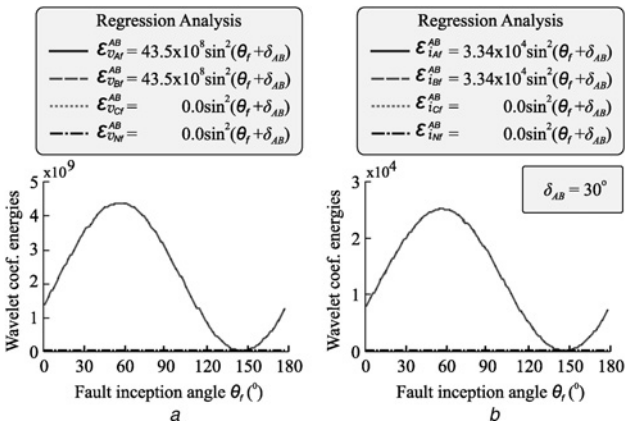

Fig. 7 *Wavelet coefficient energies of voltages and currents at fault location in AB faults*

a $\mathcal{E}^{AB}_{v_{Af}}(\theta_f)$, $\mathcal{E}^{AB}_{v_{Bf}}(\theta_f)$, $\mathcal{E}^{AB}_{v_{Cf}}(\theta_f)$, and $\mathcal{E}^{AB}_{v_{Nf}}(\theta_f)$

b $\mathcal{E}^{AB}_{i_{Af}}(\theta_f)$, $\mathcal{E}^{AB}_{i_{Bf}}(\theta_f)$, $\mathcal{E}^{AB}_{i_{Cf}}(\theta_f)$, and $\mathcal{E}^{AB}_{i_{Nf}}(\theta_f)$

instance, the energies related to the voltages at the point of the fault were

$$\mathcal{E}^{BC}_{v_{Af}} \simeq 0.0, \quad \mathcal{E}^{BC}_{v_{Bf}} \simeq 43.5 \times 10^8 \sin^2(\theta_f + \delta_{BC})$$
$$\mathcal{E}^{BC}_{v_{Cf}} \simeq 43.5 \times 10^8 \sin^2(\theta_f + \delta_{BC}) \quad \text{and} \quad \mathcal{E}^{BC}_{v_{Nf}} \simeq 0.0$$

for *BC* faults and

$$\mathcal{E}^{CA}_{v_{Af}} \simeq 43.5 \times 10^8 \sin^2(\theta_f + \delta_{CA}), \quad \mathcal{E}^{CA}_{v_{Bf}} \simeq 0.0,$$
$$\mathcal{E}^{CA}_{v_{Cf}} \simeq 43.5 \times 10^8 \sin^2(\theta_f + \delta_{CA}), \quad \text{and} \quad \mathcal{E}^{CA}_{v_{Nf}} \simeq 0.0$$

for *CA* faults. The energy waveforms regarding the LL faults were obtained with $R^2 \simeq 0.9999$.

After the analysis of the wavelet coefficient energy waveforms of *AB*, *BC* and *AC* faults, it was verified that [8]:

- The wavelet coefficient energies regarding the fault-induced transients in all voltages and currents along the line in LL faults are square sinusoidal functions of the fault inception angle according to (5).
- The wavelet coefficient energies regarding the voltages and currents in both the sound phase and neutral present the parameters $E_0 \simeq 0$ and $E_1 \simeq 0$. As a consequence, the wavelet coefficient energies (or the fault-induced transients) at line ends can be properly used for the fault classification purpose.
- The energy peak (the hardest fault-induced transients) in all energy waveforms is in accordance with the maximum value of (6): $\theta_f = 60^\circ$, $\theta_f = 0^\circ$ and $\theta_f = 120^\circ$ in *AB*, *BC* and *AC* faults, respectively.
- There is a fault inception angle where the wavelet coefficient energy values of the faulted voltages and currents are about zero (no fault-induced transients). As a consequence, in *AB* faults, for instance, algorithms based on the fault-induced transient or travelling wave analysis to detect and locate faults may fail when the fault inception angle is near 150°.
- Once the maximum line voltage is higher than the maximum phase voltage, LL faults can generate wavelet coefficient energies (and the fault-induced transients) more severe than SLG faults.

6 Fault inception angle effects in double line-to-ground faults

In order to evaluate the effects of the fault inception angle in the fault-induced transients in DLG faults, the wavelet coefficient energies at the fault location and at bus 1 were assessed. Fig. 8 depicts the energy waveforms of the currents at the fault location for *ABG* faults ($\mathcal{E}^{ABG}_{i_{Af}}$, $\mathcal{E}^{ABG}_{i_{Bf}}$, $\mathcal{E}^{ABG}_{i_{Cf}}$ and $\mathcal{E}^{ABG}_{i_{Nf}}$).

By using regression analysis through the Curve Fitting Toolbox of Matlab®, (5) was also true to the wavelet coefficient energies regarding the *ABG* (Fig. 8), *BCG* and *CAG* faults monitored at both bus 1 and the fault point. Fig. 8 depicts also the values of E_0, E_1 and δ_E obtained through the regression analysis. Regarding the *BCG* and *CAG* faults, the features of the energies were similar to *ABG* faults. For instance, the energies related to the currents

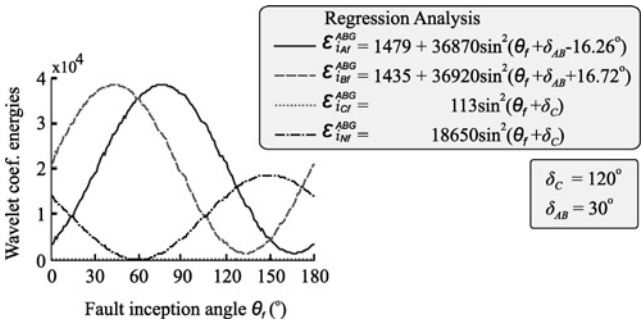

Fig. 8 *Wavelet coefficient energies of currents at the fault location regarding the ABG faults*
$\mathcal{E}^{ABG}_{i_{Af}}(\theta_f)$, $\mathcal{E}^{ABG}_{i_{Bf}}(\theta_f)$, $\mathcal{E}^{ABG}_{i_{Cf}}(\theta_f)$ and $\mathcal{E}^{ABG}_{i_{Nf}}(\theta_f)$

at the point of the fault were

$$\mathcal{E}^{BCG}_{i_{Af}} \simeq 113 \sin^2(\theta_f + \delta_A)$$
$$\mathcal{E}^{BCG}_{i_{Bf}} \simeq 1480 + 36\,870 \sin^2(\theta_f + \delta_{BC} - 16.36^\circ)$$
$$\mathcal{E}^{BCG}_{i_{Cf}} \simeq 1490 + 36\,910 \sin^2(\theta_f + \delta_{BC} + 16.52^\circ), \quad \text{and}$$
$$\mathcal{E}^{BCG}_{i_{Nf}} \simeq 18\,635 \sin^2(\theta_f + \delta_A)$$

for *BCG* faults and

$$\mathcal{E}^{CAG}_{i_{Af}} \simeq 1501 + 36\,880 \sin^2(\theta_f + \delta_{CA} + 16.63^\circ),$$
$$\mathcal{E}^{CAG}_{i_{Bf}} \simeq 114 \sin^2(\theta_f + \delta_B)$$
$$\mathcal{E}^{CAG}_{i_{Cf}} \simeq 1443 + 36930 \sin^2(\theta_f + \delta_{CA} - 16.31^\circ) \quad \text{and}$$
$$\mathcal{E}^{CAG}_{i_{Nf}} \simeq 18\,630 \sin^2(\theta_f + \delta_B)$$

for *CAG* faults. The energy waveforms regarding the DLG faults were obtained with $R^2 \simeq 0.9998$.

In contrast to SLG and LL faults, the value of the parameter δ_E is different for each phase and neutral signal in a specific DLG fault. As a consequence, the worst fault-induced transients (maximum energy value) in phase and neutral signals take place in different fault inception angles (Fig. 8). Therefore DLG faults produce fault-induced transients for all possible fault inception angles and the fault can be always detected by means of the wavelet coefficient energy analysis.

After an extensive analysis of DLG faults, it was observed that, for instance, the transient features regarding the *ABG* fault can be understood through the $AG + BG + AB$ faults striking at the same time and location. In this way, it is assumed that

$$\sum_{k=k_f}^{k_f+\Delta k} w^{ABG}_{i_{Af}}(k) = \sum_{k=k_f}^{k_f+\Delta k} (w^{AG}_{i_{Af}}(k) + w^{BG}_{i_{Af}}(k) + w^{AB}_{i_{Af}}(k)) \quad (12)$$

where $w^{\text{Type}}_{i_{Af}}$ is the wavelet coefficient of the current i_{Af}; Type indicates the type of the fault. *A* similar equation is also true for the other currents and voltages.

doi: 10.1049/iet-gtd.2011.0539

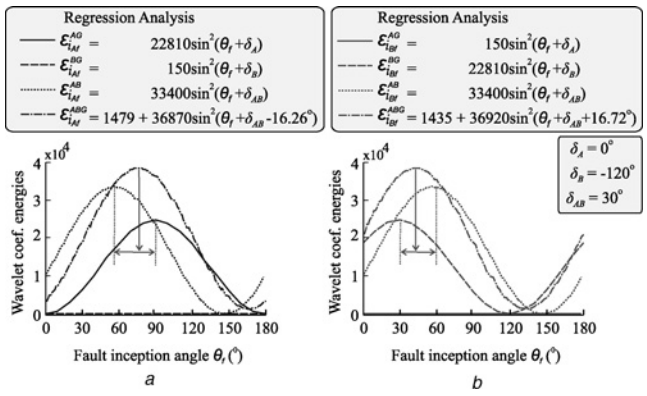

Fig. 9 *Comparison between the wavelet coefficient energy waveforms of the AG, BG, AB and ABG faults regarding the*

a Phase *A* current
b Phase *B* current

With regard to the wavelet coefficient energies, from (2) and (12), the following inequality is observed

$$\sum_{k=k_f}^{k_f+\Delta k} |w_{i_{Af}}^{ABG}(k)|^2 \neq \sum_{k=k_f}^{k_f+\Delta k} (|w_{i_{Af}}^{AG}(k)|^2 + |w_{i_{Af}}^{BG}(k)|^2 + |w_{i_{Af}}^{AB}(k)|^2) \quad (13)$$

Even through $\mathcal{E}_{i_{Af}}^{ABG} \neq \mathcal{E}_{i_{Af}}^{AG} + \mathcal{E}_{i_{Af}}^{BG} + \mathcal{E}_{i_{Af}}^{AB}$, the features of $\mathcal{E}_{i_{Af}}^{ABG}$ can be understood by comparison with $\mathcal{E}_{i_{Af}}^{AG}$, $\mathcal{E}_{i_{Af}}^{BG}$, and $\mathcal{E}_{i_{Af}}^{AB}$. Fig. 9 depicts the wavelet coefficient energies of the phase A and B currents at the fault location for the simulated *AG*, *BG*, *AB* and *ABG* faults.

According to Fig. 9, taking into account the same fault resistance, fault location and system load, the maximum value of the wavelet coefficient energies is greater in DLG faults. In other words, the fault-induced transients in DLG can be more severe than the SLG and LL faults.

With regard to an *ABG* fault (Fig. 9), the worst fault-induced transients at phase *A* current (or voltage) are expected to be between 60° (the worst fault-induced transients in *AB* faults) and 90° (the worst fault-induced transients in *AG* faults). On the other hand, the worst fault-induced transients at phase *B* current (or voltage) are expected to be between 30° (the worst fault-induced transients in BG faults) and 60°. In addition, at a fault inception angle of 60° (Fig. 8), the energy of the fault-induced transients is the same in phase *A* and *B* currents (and voltages) and there are no fault-induced transients in phase *C* and neutral signals. In this case, under the transient point of view, an *ABG* fault presents features such as an *AB* fault.

The fault-induced transients in DLG faults can be used for fault classification because of the fact that the energies related to the fault and neutral signals are greater than the energy of the sound signal. However, there is a fault inception angle in which a DLG fault may be classified as LL fault.

7 Fault inception angle effects in three line faults

In order to identify the effects of the fault inception angle in fault-induced transients of *ABC* faults, the wavelet coefficient energies at the fault location and at bus 1 were assessed. Fig. 10 depicts the energy waveforms at the fault location.

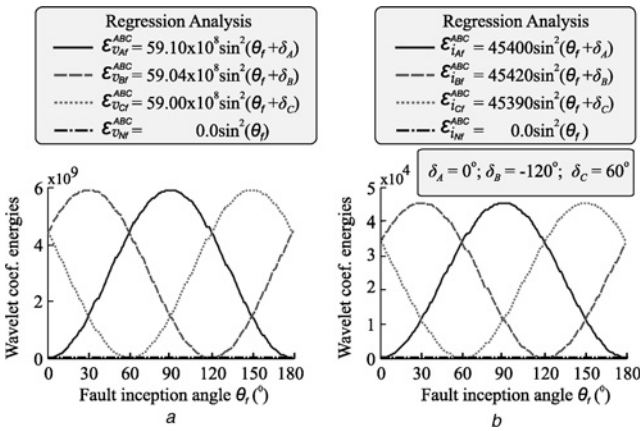

Fig. 10 *Wavelet coefficient energies of the voltages and currents at the fault location regarding the ABC faults*

a $\mathcal{E}_{v_{Af}}^{ABC}(\theta_f)$, $\mathcal{E}_{v_{Bf}}^{ABC}(\theta_f)$, $\mathcal{E}_{v_{Cf}}^{ABC}(\theta_f)$ and $\mathcal{E}_{v_{Nf}}^{AB}(\theta_f)$
b $\mathcal{E}_{i_{Af}}^{ABC}(\theta_f)$, $\mathcal{E}_{i_{Bf}}^{ABC}(\theta_f)$, $\mathcal{E}_{i_{Cf}}^{ABC}(\theta_f)$ and $\mathcal{E}_{i_{Nf}}^{ABC}(\theta_f)$

By using regression analysis through the Curve Fitting Toolbox of Matlab®, (5) was also true to the wavelet coefficient energies of the voltages and currents at the fault location in *ABC* faults, with hardest transients in voltages and currents at phases *A*, *B* and *C* when $\theta_f = 90°$, $\theta_f = 30°$ and $\theta_f = 150°$, respectively. In addition, $\mathcal{E}_{v_{Nf}}^{ABC} \simeq 0$ and $\mathcal{E}_{i_{Nf}}^{ABC} \simeq 0$. Fig. 10 also depicts the values of E_1 and δ_E obtained through regression analysis. The energy waveforms regarding the *ABC* faults were obtained with $R^2 \simeq 0.9999$.

According to Fig. 10, the wavelet coefficient energies of the signals are phase-shifted by 60 electrical degrees. In this way, at least two wavelet coefficient energies in voltages (and currents) are different from zero in all fault inception angles. As a consequence, the fault can always be detected by means of the fault-induced transient analysis (wavelet coefficient energy or transient energy analysis). Under transient point of view, around $\theta_f = 0°$, 60° and 120° an *ABC* fault presents similar features of a *BC*, *AB* and *AC* fault, respectively. In these cases, the energy values in two phase voltages (currents) are the same and the energy value of a third phase voltage (current) is null. In other words, a three line fault can be classified as LL fault at fault inception angles of 0°, 60° and 120° by means of the fault-induced transient analysis.

8 Practical applications

Fig. 11 depicts the phase A voltage and current, at bus 1, as well as their wavelet coefficient energies at the first scale, respectively, of a simulated *AG* fault with $\theta_f = 90°$. The energies were computed with a one-cycle energy window, by using (2), which was shifted sample-by-sample. As expected, instead of k_f, the fault-induced transients are observed from sample k_1, where the phase angle in v_A is $\theta_f + \Delta\theta$.

During the steady-state system operation ($k < k_1$) the energies are because of noises and present value almost constant (Figs. 11*c* and *d*). However, there is a hard increasing of energy from sample k_1 in each energy waveform. In this way, the fault can be detected at sample k_1 and the phase angle $\theta_f + \Delta\theta$ can be estimated at phase *A* voltage.

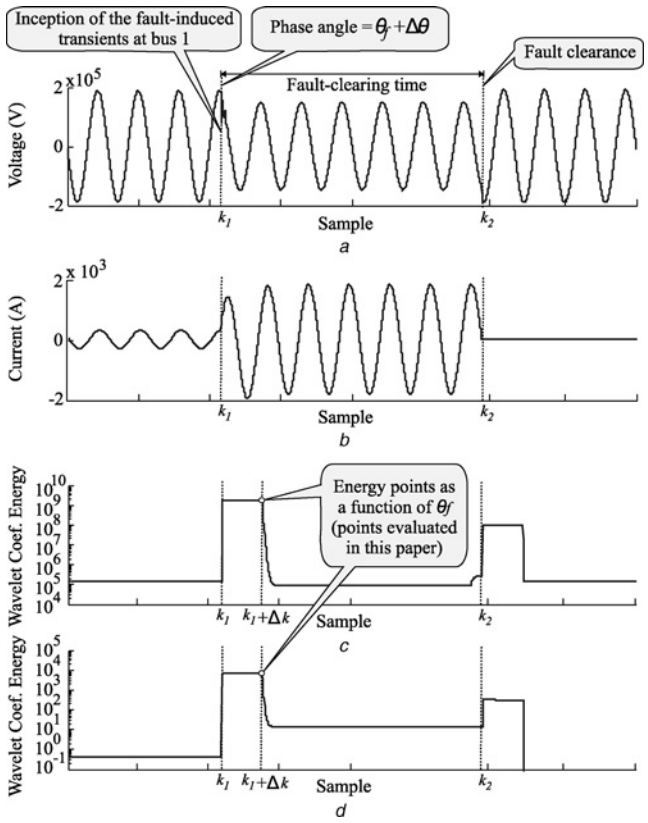

Fig. 11 *Oscillographic record at bus 1 with an AG fault*

a v_A
b i_A
c $\mathcal{E}_{v_A}^{AG}$
d $\mathcal{E}_{i_A}^{AG}$

In this paper, only the energies at sample $k_1 + \Delta k$ (Figs. 11*c* and *d*) were dealt with. However, the energies during all the first cycle after the fault ($\mathcal{E}(k_1 \leq k \leq k_1 + \Delta k)$) present similar features as energies at sample $k_1 + \Delta k$: the energies soon after the inception of the fault-induced transients are function of θ_f according to (5). As a consequence, the fault can be classified through the analysis of the wavelet coefficient energies from the first sample after the fault detection.

If $\theta_f + \Delta\theta$ can be estimated at fault-induced transient detection and θ_f can be estimated by comparing the post-fault energies with (5), the fault can be located by using $\Delta\theta$ and the propagation time of the travelling waves.

According to [9], the wavelet coefficients of db4 wavelet can be easily computed in real-time. As a consequence, the energies $\mathcal{E}_{v_A}$, $\mathcal{E}_{v_B}$, $\mathcal{E}_{v_C}$, $\mathcal{E}_{v_N}$, $\mathcal{E}_{i_A}$, $\mathcal{E}_{i_B}$, $\mathcal{E}_{i_C}$ and $\mathcal{E}_{i_N}$ can also be computed in real-time. However, in case of a wavelet-based method to detect, classify and locate faults the best mother wavelet must be identified owing to the effectiveness of the wavelet analysis may be influenced by the choice of the mother wavelet.

The advantage of the analysis of the wavelet coefficient energies in real-time is the high-speed fault detection, classification and location in satisfactory agreement with real application in protective relays [8]. The real-time fault diagnosis is not dealt with in this paper.

The disadvantage of the real-time analysis of the wavelet coefficient energies is that SLG and LL faults can not present fault-induced transients in some specific fault inception angles. Most methods based on both travelling waves and transient analysis may fail in these cases [11]. However, from a statistical point of view faults appear more often at voltages large enough to initiate the insulation breakdown (close to the maximum point on wave). Therefore the cases where the energies of the wavelet coefficients do not present a significant increase are unusual.

The effects of the fault resistance and location in the fault-induced transients for each type of fault as well as the analysis of simultaneous and developing faults by using the proposed wavelet-based methodology can be performed in future papers.

9 Conclusions

The effects of the fault inception angle in the energy of the fault-induced transients in both voltages and currents were evaluated by means of the wavelet coefficient energy analysis.

The wavelet coefficient energies regarding the fault-induced transients (energies of the fault-induced transients) in all voltages and currents, in all faults, are square sinusoidal functions of the fault inception angle. These energies present particular features according to the fault type, as follows:

- SLG faults: the energy peak (the worst fault-induced transient condition) in all voltages and currents corresponds to the fault striking in the faulted phase voltage peak. There is a fault inception angle where the wavelet coefficient energy values in all voltages and currents are about zero (no fault-induced transients).
- LL faults: the energy peak in faulted phase voltages and currents corresponds to the fault striking in the faulted line voltage peak. There is a fault inception angle where the wavelet coefficient energy values in faulted phase voltages and currents are about zero (no fault-induced transients). With regard to sound phase and neutral, the wavelet coefficient energy values are about zero for all fault inception angle.
- DLG faults: In all possible fault inception angles, the wavelet coefficient energy values are different from zero at least in two voltages (currents). There are some specific fault inception angle values where the wavelet coefficient energies regarding the fault-induced transients in DLG faults present similar features of LL faults.
- Three line faults: In all possible fault inception angles, the wavelet coefficient energy values are different from zero at least in two voltages (currents). There are some specific fault inception angle values where the wavelet coefficient energies regarding the fault-induced transients in three line faults present similar features of LL faults.

The wavelet coefficient energies regarding the fault-induced transients at line ends can be used for fault detection, classification and location purposes. However, in SLG faults and LL faults there are specific fault inception angles in which the fault-induced transients are very damped. In this case, the transient-based methods for fault detection can fail. With regard to transient-based methods for fault classification, there are also some fault inception angles in which a double-line-to-ground fault or a three line fault can be classified as LL fault.

The wavelet coefficient energies can be computed in real-time taking into account the last wavelet coefficients into a fixed window length. In this way, the fault-induced transient analysis can provide a high-speed fault detection,

doi: 10.1049/iet-gtd.2011.0539

classification and location in accordance with the protective relay applications.

10 Acknowledgment

This work was supported by Brazilian National Research Council (CNPq).

11 References

1 Tleis, N.: 'Power systems modelling and fault analysis: theory and practice' (Newnes, Elsevier Ltd., London, UK, 2008)
2 Horowitz, S.H., Phadke, A.G.: 'Power system relaying' (John Wiley & Sons Inc., New York, USA, 2008)
3 Anderson, P.M.: 'Power system protection' (IEEE Press Series on Power Engineering, Piscataway, NJ, USA, 1999)
4 Vzquez-Martnez, E.: 'A travelling wave distance protection using principal component analysis', *Int. J. Electr. Power Energy Syst.*, 2003, **25**, (6), pp. 471–479
5 Bradley, A.D., Gray, C.B., O'Kelly, D.: 'Transient compensation of current transformers', *IEEE Trans. Power Appar. Syst.*, 1978, **PAS-97**, (4), pp. 1264–1271
6 Swift, G.W.: 'The spectra of fault-induced transients', *IEEE Trans. Power Appar. Syst.*, 1979, **PAS-98**, (3), pp. 940–947
7 Johns, A.T., Aggarwal, R.K., Bo, Z.Q.: 'Non-unit protection technique for ehv transmission systems based on faultgenerated noise, part 1: Signal measurement', *IEE Proc. Gener. Transm. Distrib.*, 1994, **141**, (2), pp. 133–140
8 Costa, F.B.: 'Uma técnica de diagnóstico em tempo real de distúrbios transitórios baseada na transformada wavelet para uso em registradores digitais de perturbação'. PhD dissertation, Federal University of Campina Grande, Campina Grande, Brazil, 2010
9 Costa, F.B., Souza, B.A., Brito, N.S.D.: 'Real-time detection of fault-induced transients in transmission lines', *IET Electron. Lett.*, 2010, **46**, (11), pp. 753–755
10 Upendar, J., Gupta, C.P., Singh, G.K., Ramakrishna, G.: 'PSO and ann-based fault classification for protective relaying', *IET Gener. Transm. Distrib.*, 2010, **4**, (10), p. 11971212
11 Kale, V.S., Bhide, S.R., Bedekar, P.P.: 'Faulted phase selection based on wavelet analysis of traveling waves', *Int. J. Comput. Electr. Eng.*, 2011, **3**, (3), pp. 421–425
12 Zhang, D.-J., Wu, Q.H., Bo, Z.Q., Caunce, B.: 'Transient positional protection of transmission lines using complex wavelets analysis', *IEEE Trans. Power Deliv.*, 2003, **18**, (3), pp. 705–710
13 Valsan, S.P., Swarup, K.: 'Wavelet transform based digital protection for transmission lines', *Int. J. Electr. Power Energy Syst.*, 2009, **31**, (78), pp. 379–388
14 Daubechies, I.: 'Ten lectures on wavelets' (CBMS-NSF Regional Conference Series, SIAM, Philadelphia, USA, 1992)
15 Percival, D.B., Walden, A.T.: 'Wavelet methods for time series analysis' (Cambridge University Press, 2000)
16 Bollen, M.H.J., Gu, I.Y.-H.: 'Signal processing of power quality disturbances' (IEEE, New York, USA, 2006)